

1 **K18-hACE2 mice develop respiratory disease resembling severe COVID-19**

2

3 Claude Kwe Yinda<sup>1\*</sup>, Julia R. Port<sup>1\*</sup>, Trenton Bushmaker<sup>1\*</sup>, Irene Offei Owusu<sup>1</sup>, Victoria A.  
4 Avanzato<sup>1</sup>, Robert J. Fischer<sup>1</sup>, Jonathan E. Schulz<sup>1</sup>, Myndi G. Holbrook<sup>1</sup>, Madison J. Hebner<sup>1</sup>,  
5 Rebecca Rosenke<sup>2</sup>, Tina Thomas<sup>2</sup>, Andrea Marzi<sup>1</sup>, Sonja M. Best<sup>1</sup>, Emmie de Wit<sup>1</sup>, Carl Shaia<sup>2</sup>,  
6 Neeltje van Doremalen<sup>1</sup>, Vincent J. Munster<sup>1#</sup>.

7

8 *1. Laboratory of Virology, National Institute of Allergy and Infectious Diseases, National*  
9 *Institutes of Health, Hamilton, MT, USA.*

10 *2. Rocky Mountain Veterinary Branch, National Institute of Allergy and Infectious*  
11 *Diseases, National Institutes of Health, Hamilton, MT, USA*

12

13 \*Joint first authors

14 #corresponding author

## 15 **Abstract**

16 SARS-CoV-2 emerged in late 2019 and resulted in the ongoing COVID-19 pandemic. Several  
17 animal models have been rapidly developed that recapitulate the asymptomatic to moderate disease  
18 spectrum. Now, there is a direct need for additional small animal models to study the pathogenesis  
19 of severe COVID-19 and for fast-tracked medical countermeasure development. Here, we show  
20 that transgenic mice expressing the human SARS-CoV-2 receptor (angiotensin-converting enzyme  
21 2 [hACE2]) under a cytokeratin 18 promoter (K18) are susceptible to SARS-CoV-2 and that  
22 infection resulted in a dose-dependent lethal disease course. After inoculation with either  $10^4$   
23 TCID<sub>50</sub> or  $10^5$  TCID<sub>50</sub>, the SARS-CoV-2 infection resulted in rapid weight loss in both groups and  
24 uniform lethality in the  $10^5$  TCID<sub>50</sub> group. High levels of viral RNA shedding were observed from  
25 the upper and lower respiratory tract and intermittent shedding was observed from the intestinal  
26 tract. Inoculation with SARS-CoV-2 resulted in upper and lower respiratory tract infection with  
27 high infectious virus titers in nasal turbinates, trachea and lungs. The observed interstitial  
28 pneumonia and pulmonary pathology, with SARS-CoV-2 replication evident in pneumocytes,  
29 were similar to that reported in severe cases of COVID-19. SARS-CoV-2 infection resulted in  
30 macrophage and lymphocyte infiltration in the lungs and upregulation of Th1 and proinflammatory  
31 cytokines/chemokines. Extrapulmonary replication of SARS-CoV-2 was observed in the cerebral  
32 cortex and hippocampus of several animals at 7 DPI but not at 3 DPI. The rapid inflammatory  
33 response and observed pathology bears resemblance to COVID-19. Taken together, this suggests  
34 that this mouse model can be useful for studies of pathogenesis and medical countermeasure  
35 development.

36

37

## 38 **Authors Summary**

39 The disease manifestation of COVID-19 in humans range from asymptomatic to severe. While  
40 several mild to moderate disease models have been developed, there is still a need for animal  
41 models that recapitulate the severe and fatal progression observed in a subset of patients. Here, we  
42 show that humanized transgenic mice developed dose-dependent disease when inoculated with  
43 SARS-CoV-2, the etiological agent of COVID-19. The mice developed upper and lower  
44 respiratory tract infection, with virus replication also in the brain after day 3 post inoculation. The  
45 pathological and immunological diseases manifestation observed in these mice bears resemblance  
46 to human COVID-19, suggesting increased usefulness of this model for elucidating COVID-19  
47 pathogenesis further and testing of countermeasures, both of which are urgently needed.

48

## 49 **Introduction**

50 Severe acute respiratory syndrome coronavirus-2 (SARS-CoV-2) emerged in Hubei province in  
51 mainland China in December 2019, and is the etiological agent of coronavirus disease (COVID)-  
52 19 (1). SARS-CoV-2 can cause asymptomatic to severe lower respiratory tract infections in  
53 humans, with early clinical signs including fever, cough and dyspnea (2, 3). Progression to severe  
54 disease may be marked by acute respiratory distress syndrome (ARDS), with pulmonary edema,  
55 bilateral diffuse alveolar damage and hyaline membrane formation (4-6). Although primarily a  
56 respiratory tract infection, extra-respiratory replication of SARS-CoV-2 has been observed in  
57 kidney, heart, liver and brain in fatal cases (7-9). Several experimental animal models for SARS-  
58 CoV-2 infection have been developed, including hamsters (10) ferrets (11) and non-human primate  
59 models (12-15). SARS-CoV-2 pathogenicity within these animal models ranges only from mild to  
60 moderate (10-15). Additional small animal models that recapitulate more severe disease

61 phenotypes and lethal outcome are urgently needed for the rapid pre-clinical development of  
62 medical countermeasures. Although the SARS-CoV-2 spike glycoprotein is able to utilize hamster  
63 angiotensin-converting enzyme 2 (ACE2) as the receptor of cell entry (10, 16), lack of species-  
64 specific reagents limit the usability of this model. As SARS-CoV-2 is unable to effectively utilize  
65 murine (m)ACE2 (17, 18), several models are currently under development to overcome this  
66 species barrier using a variety of strategies including transiently expressed human (h)ACE2,  
67 CRISPR/Cas9 modified mACE2, exogenous delivery of hACE2 with a replication-deficient viral  
68 vector and mouse-adapted SARS-CoV-2 (19-23).

69 K18-hACE2 transgenic mice were originally developed as a small animal model for lethal SARS-  
70 CoV infection. Expression of hACE2 is driven by a cytokeratin promoter in the airway epithelial  
71 cells as well as in epithelia of other internal organs, including the liver, kidney, gastrointestinal  
72 tract and brain. Infection with SARS-CoV led to severe interstitial pneumonia and death of the  
73 animals by day 7 post inoculation (20). Here, we assess the susceptibility of K18-hACE2  
74 transgenic mice as a model of severe COVID-19.

75

## 76 **Results**

### 77 **Disease manifestation in SARS-CoV-2-inoculated K18-hACE2 mice**

78 First, we determined the disease progression after SARS-CoV-2 inoculation. Two groups of 4-6  
79 week-old K18-hACE2 transgenic male and female mice (15 each) were intranasally inoculated  
80 with  $10^4$  (low dose group) and  $10^5$  (high dose group) TCID<sub>50</sub> SARS-CoV-2, respectively. In  
81 addition, one control group of two mice was intranasally inoculated with  $10^5$  TCID<sub>50</sub>  $\gamma$ -irradiated  
82 SARS-CoV-2.

83 Irrespective of SARS-CoV-2 inoculation dose, mice uniformly started losing weight at 2 days post  
84 inoculation (DPI) (Fig 1a), with a significantly higher weight loss observed in the low dose group,  
85 suggesting a dose-response relationship, ( $p = 0.02$ , Wilcoxon matched-pairs rank test). No  
86 difference in weight loss between male and female animals within the same dose group was  
87 detected (S1a Fig). In addition to weight loss, lethargy, ruffled fur, hunched posture and labored  
88 breathing were observed throughout the course of infection in each animal. Mice were monitored  
89 for signs of neurological disease (circling, rolling, hyperexcitability, convulsions, tremors,  
90 weakness, or flaccid paralysis of hind legs), and no neurological symptoms were observed in any  
91 of the animals. Within the high dose group all animals reached euthanasia criteria by 7 DPI,  
92 however, in the low dose group five out of six animals reached euthanasia criteria 5-9 DPI and one  
93 animal recovered (Fig 1b). Although, no sex-dependent differences in survival were observed  
94 between male and female mice, the animal size used in this study was too small to draw major  
95 conclusions (S1b Fig). The control animals inoculated with  $\gamma$ -irradiated SARS-CoV-2 did not lose  
96 weight and remained free of disease symptoms.

97

### 98 **Viral shedding in SARS-CoV-2-inoculated K18-hACE mice**

99 To gain an understanding of dose-dependent virus shedding patterns of SARS-CoV-2 in infected  
100 K18-hACE2 mice, daily nasal, oropharyngeal and rectal swabs were obtained until 11 DPI. Viral  
101 RNA was detected in all three. SARS-CoV-2 shedding from the respiratory tract was observed in  
102 all inoculated animals. Viral load in oropharyngeal and nasal swabs reached up to  $\sim 10^6$  and  $\sim 10^7$   
103 copies/mL, respectively, and viral RNA could be detected up to 7 and 8 DPI. Rectal shedding was  
104 observed in both inoculated groups, but not in all animals, and was lower compared to respiratory  
105 shedding. Importantly, no viral RNA could be detected in swabs obtained from control mice

106 inoculated with  $\gamma$ -irradiated SARS-CoV-2, suggesting viral RNA detected as early as 1 DPI was  
107 directly associated with active virus replication and did not originate from inoculum (Fig 1c). No  
108 sex-dependent differences in shedding pattern were seen (S1c Fig).

109

### 110 **Tissue tropism of SARS-CoV-2-inoculated K18-hACE mice**

111 We next assessed tissue tropism and viral replication of SARS-CoV-2 in K18-hACE2 mice (Fig  
112 2a). Viral genomic RNA was detected in almost all tissues; however, no viremia was observed. At  
113 3 and 7 DPI, the highest viral load was found in lung tissue ( $\sim 10^{10}$  genome copies/g). Viral RNA  
114 in brain tissue was increased at 7 DPI compared to 3 DPI (from  $\sim 10^5$  to  $10^{10}$  genome copies/g) (Fig  
115 2a). When assessing infectious virus, at 3 DPI, it was only detected in respiratory tract tissues,  
116 with high infectious titers observed in nasal epithelium and lungs in both the low dose and high  
117 dose groups. At 7 DPI, infectious virus was detected in respiratory tract as well as brain tissue  
118 (Figs 2b). Together, these data suggest that either SARS-CoV-2 is initially exclusively targets the  
119 respiratory tract in K18-hACE2 mice with secondary central nervous system (CNS) involvement  
120 or the virus replicates slower in the brain and only detected after 3 DPI.

121

### 122 **Histological changes and viral antigen distribution in SARS-CoV-2-inoculated K18-hACE** 123 **mice**

124 On 3 and 7 DPI, four animals from each group were euthanized and necropsies were performed.  
125 On both days, gross lung lesions were observed in all animals with up to 80% of the lungs affected  
126 by 7 DPI. Histologically, all animals developed pulmonary pathology after inoculation with  
127 SARS-CoV-2. Lungs showed interstitial pneumonia at 3 DPI characterized by a generalized  
128 perivascular infiltration of inflammatory cells including neutrophils, macrophages and

129 lymphocytes; alveolar septal thickening, and distinctive vascular system injury (Fig 3a-3c). At 7  
130 DPI, mice developed pulmonary pathology consisting of multifocal interstitial pneumonia  
131 characterized by type II pneumocyte hyperplasia, septal, alveolar and perivascular inflammation  
132 comprised of lymphocytes, macrophages and neutrophils, variable amounts of alveolar fibrin and  
133 edema, frequent syncytial cells and single cell necrosis. Terminal bronchioles were similarly  
134 affected and in the most severely affected areas fibrin and necrosis occluded the lumen (Fig 3e-  
135 3g). Immunohistochemistry (IHC) demonstrated viral antigen in pneumocytes and macrophages  
136 of tissues on both 3 and 7 DPI (Fig 3d-3h).

137 We evaluated the localized infiltration of innate and adaptive immune cell populations at 3 and 7  
138 DPI, as compared to control animals and the survivor at 21 DPI. An absence of immunoreactive  
139 macrophages (CD68+) in the  $\gamma$ -irradiated SARS-CoV-2 inoculated controls was noted (Fig 4a). In  
140 contrast, in lung tissue of infected animals, an infiltration of a limited number of macrophages at  
141 3 and 7 DPI was seen, which persisted in the survivor up until 21 DPI (Fig 4 d, g and j). We next  
142 assessed lymphocyte infiltration into the lung in more detail. T cells were present in low numbers  
143 in the non-infected control (Fig 4b). At 3 DPI T cells numbers increases in perivascular tissue and  
144 alveolar septa and persisted through 7 DPI. B cells were present in low numbers in the  $\gamma$ -irradiated  
145 SARS-CoV-2 inoculated controls and at 3 DPI, increased numbers were observed in alveolar septa.  
146 B cells persisted through 7 DPI, when they started to cluster and form aggregates. At 21 DPI, T  
147 cells were found throughout the whole lung section and formation of lymphoid aggregates with B  
148 cells in perivascular tissues was observed in the survivor (Fig 4e, h and k). Interestingly, this  
149 animal also still demonstrated mildly inflamed alveolar septa which were often accompanied by  
150 foamy macrophages within affected alveoli (S2 Fig).

151 Both SARS-CoV-2 inoculated groups showed only limited lesions in the nasal turbinates at 3 and  
152 7 DPI (Fig 5a-5b). IHC showed multifocal SARS-CoV-2 antigen in ciliated respiratory epithelial  
153 cells (Fig 5c-5d).

154 At 3 DPI all brains were histologically normal (Fig 6a-6b). However, 7 DPI brain tissues showed  
155 lesions ranging from minimal to moderate and included lymphocytic perivascular cuffing, gliosis,  
156 meningitis, encephalitis and microthrombi, a generalized increase in cellularity of the meninges,  
157 cerebral cortex and hippocampus and presence of edema (Fig 6c-6d). Abundant SARS-CoV-2  
158 antigen was detected in the cerebral cortex and hippocampus within neurons and glial cells along  
159 the soma and axons (Fig 6e-6f). In addition, cerebral cortex contained microthrombi and an  
160 increased glial cell count, infiltration of inflammatory cells and scant hemorrhage (Fig 6g-6f).

161

#### 162 **Rapid humoral immune response in SARS-CoV-2-inoculated K18-hACE mice**

163 We next investigated two key aspects of the anti-viral immune response. To assess B-cell response  
164 and class-switch, the presence of SARS-CoV-2 spike-specific immunoglobulin (Ig)G and IgM  
165 antibodies in serum obtained at 3 and 7 DPI was investigated using ELISA. By 3 DPI, one mouse  
166 in the high dose group was positive for IgM and no mice were positive for IgG. In contrast, both  
167 spike-specific IgM and IgG were found in sera of all mice at 7 DPI (Fig 7a). IgM and IgG titers of  
168 one surviving animal at 21 DPI were comparable to those at 7 DPI.

169

#### 170 **Rapid systemic upregulation of proinflammatory cytokines and chemokines in SARS-CoV-2-** 171 **inoculated K18-hACE mice**

172 To investigate the immune response further we utilized serum multiplex cytokine analysis to  
173 characterize the inflammatory status and identify key patterns. Interestingly, while serum cytokine



174 levels at 3 DPI showed only slight changes as compared to control animals, strong upregulation  
175 was observed for multiple cytokines and chemokines by 7 DPI (Fig 7b). A strong increase in T  
176 helper (Th)1-mediated cytokines interferon (IFN)- $\gamma$  (both doses,  $p = 0.0268, 0.0268$ ) and tumour  
177 necrosis factor (TNF)- $\alpha$ , (though not statistically significant) was observed. In addition, there was  
178 also an upregulation of proinflammatory and chemoattractant cytokine IFN- $\gamma$ -induced protein (IP)-  
179 10 (C-X-C motif chemokine ligand (CXCL10)) (high dose,  $p = 0.0268$ ). Interestingly, no trend of  
180 upregulation of Th2 anti-inflammatory cytokines interleukin (IL)-4 and IL-5 was seen, but  
181 increased levels of IL-10 were observed at DPI 7 in both groups, which has been shown to have an  
182 anti-inflammatory regulatory function in mediating antiviral responses (24). In addition, granulocyte-  
183 macrophage colony-stimulating factor (GM-CSF), KC (CXCL1) and monocyte chemoattractant  
184 protein-1 (MCP-1 (C-C motif chemokine ligand (CCL1))) were detected systemically and at increased  
185 levels at 7 DPI, further indicating a systemic recruitment of inflammatory and innate immune cells to  
186 sites of infection (Fig 3a and S2a Fig). Of note, this model did not recapitulate the increase of systemic  
187 IL-6 observed in severe COVID-19 patients (25) in either dose or timepoint. When comparing the  
188 overall cytokine profile of each animal, it became obvious that there was a stronger link between time  
189 post inoculation than between the viral dose and the resulting cytokine upregulation. We observed 3  
190 clusters, which showed a clear time-correlation and did not detect significant differences between  
191 low and high dose inoculated animals (Fig 7c). Correlation of serum cytokine expression with lung  
192 viral gRNA did not reveal any significant positive correlation (S2b Fig).

193

## 194 **Discussion**

195 In humans, COVID-19 has a broad clinical spectrum ranging from asymptomatic to severe disease  
196 (4-6, 25). Wildtype mice are not susceptible to infection with SARS-CoV-2 due to an inability of

197 mACE2 to facilitate sufficient cellular entry (17, 18). Based on existing lethal mouse models for  
198 SARS-CoV, first described by McCray and colleagues (20), several transgenic mouse models for  
199 COVID-19 have been developed using expression of hACE2 (21, 26-29). However, mice  
200 expressing hACE2 under the mACE2 promoter (21, 26) or exogenously transfected with hACE2  
201 showed only moderate disease with slight weight loss, reduced lung pathology and no lethal  
202 phenotype (27, 29). A mouse model expressing hACE2 under a lung ciliated epithelial cell HFH4  
203 promoter exhibited generally only mild symptoms with lethality observed only in animals with  
204 brain infection (28). In contrast, the K18-hACE2 mouse model described here, which expresses  
205 hACE2 under the K18 epithelial promoter, displayed a high morbidity and mortality in both high  
206 dose and low dose groups. These findings are corroborated by two other studies, currently in  
207 preprint (30, 31), which demonstrate a similar disease phenotype in this model.

208 Previous experiments in different hACE2 mice have demonstrated varying degrees of lung  
209 pathology upon infection with SARS-CoV-2 (19, 21-23). The K18-hACE2 mice developed  
210 edema-associated acute lung injury similar to the clinical features of COVID-19 patients, including  
211 histological aspects of ARDS. This is in line with observations made in HFH4-hACE2 mice and  
212 mice expressing hACE2 under control of the murine ACE2 promoter, where viral RNA was also  
213 detected in brain tissues (28). Severe COVID-19 is histologically characterized by diffuse alveolar  
214 damage with hyaline membranes, edema, fibrin deposits, multinucleated cells, type II pneumocyte  
215 hyperplasia and lymphocyte infiltration composed of a mixture of CD4 and CD8 lymphocytes (32-  
216 34). The analyses of the pathological response observed within the lungs of the SARS-CoV-2  
217 infected mice resemble those observed in humans with regards to lesions and cell tropism.

218 In humans, systemic cytokine response to SARS-CoV-2 infection are comprised of TNF- $\alpha$ , IL-1 $\beta$ ,  
219 IL-1R $\alpha$ , sIL-2R $\alpha$ , IL-6, IL-10, IL-17, IL-18, IFN- $\gamma$ , MCP-3, M-CSF, MIP-1 $\alpha$ , G-CSF, IP-10, and

220 MCP-1 (35-37). In the lungs of aged hACE2 mice, SARS-CoV-2 infection leads to elevated  
221 cytokine production including Eotaxin, G-CSF, IFN- $\gamma$ , IL-9, and MIP-1 $\beta$  (38). Here, we show that  
222 SARS-CoV-2 infection of K18-hACE2 mice elicits a measurable systemic pro-inflammatory  
223 cytokine response which is significantly increased at 7 DPI and characterized by an increase in  
224 IFN- $\gamma$ , TNF- $\alpha$  and IP-10, and also encompasses upregulation of innate cell-recruiting chemokines  
225 GM-CSF and MCP-1. Importantly, increased levels of IFN- $\gamma$ , IP-10, MCP-1 and TNF- $\alpha$  are  
226 associated with severity of disease in in COVID-19 patients (35, 39, 40). COVID-19 patients also  
227 show heightened IL-4 and IL-10 levels, cytokines associated with inhibitory inflammatory  
228 responses (41). While the K18-hACE2 model did not recapitulate IL-4 upregulation, increased IL-  
229 10 levels were observed in serum, suggesting that both pro- and anti-inflammatory cytokine  
230 response are functioning in this mouse model. This is particularly relevant, as in COVID-19, the  
231 resulting cytokine storm is not only thought to be detrimental to disease progression but also  
232 closely linked to the development of ARDS (39). In addition, cytokine levels are also reported to  
233 be indicative of extrapulmonary multiple-organ failure (42, 43). Reports suggest that upregulation  
234 of IL-6, IL-8, and TNF- $\alpha$  contributes to SARS-related ARDS (35, 44). Interestingly, while we did  
235 observe the upregulation of TNF- $\alpha$ , IL-6 levels remained unchanged. This needs to be further  
236 investigated to clarify if our observation suggests a differently modulated immune response and  
237 pathogenesis that should be considered for intervention studies.

238 We have also demonstrated a functional humoral immune response and production of both IgM  
239 and IgG antibodies. This is in line with observations made in ACE2-HB-01 mice where IgG  
240 antibodies against spike protein of SARS-CoV-2 were also observed (26). This indicates that the  
241 K18-hACE2 mouse model mounts a robust innate and adaptive immune response.

242 The mouse model presented here recapitulates histopathological findings of COVID-19 associated  
243 ARDS, a robust innate and adaptive immune-response, neurological involvement and, importantly,  
244 presents a dose-dependent sub-lethal disease manifestation. As such, we believe this model to be  
245 highly suitable for testing of SARS-CoV-2 countermeasures such as antiviral and immune-  
246 modulatory interventions. However, COVID-19 associated ARDS in patients presents not just  
247 with characteristic lung pathology, but also with clinical manifestations including hypoxia, loss of  
248 lung compliance and requirement for intubation, liver and kidney involvement and associated  
249 increase in serum protein levels, and decreased lymphocyte numbers. To accurately assess how  
250 well K18-hACE2 mice recapitulates human ARDS, additional studies specifically addressing  
251 these aspects are required.

252

## 253 **Materials and Methods**

### 254 **Ethics Statement**

255 Animal experiment approval was provided by the Institutional Animal Care and Use Committee  
256 (IACUC) at Rocky Mountain Laboratories. Animal experiments were executed in an Association  
257 for Assessment and Accreditation of Laboratory Animal Care (AALAC)-approved facility by  
258 certified staff, following the basic principles and guidelines in the NIH Guide for the Care and Use  
259 of Laboratory Animals, the Animal Welfare Act, United States Department of Agriculture and the  
260 United States Public Health Service Policy on Humane Care and Use of Laboratory Animals. The  
261 Institutional Biosafety Committee (IBC) approved work with infectious SARS-CoV-2 virus strains  
262 under BSL3 conditions. All sample inactivation was performed according to IBC approved  
263 standard operating procedures for removal of specimens from high containment.

264

265 **Cells and virus**

266 SARS-CoV-2 strain nCoV-WA1-2020 (MN985325.1) was provided by CDC, Atlanta, USA. Virus  
267 propagation was performed in VeroE6 cells in DMEM supplemented with 2% fetal bovine serum,  
268 1 mM L-glutamine, 50 U/mL penicillin and 50 µg/mL streptomycin. VeroE6 cells were maintained  
269 in DMEM supplemented with 10% fetal bovine serum, 1 mM L-glutamine, 50 U/mL penicillin  
270 and 50 µg/mL streptomycin.

271

272 **Animal experiments**

273 Four to six week-old male and female (15 animals each) transgenic K18-hACE2 mice expressing  
274 hACE2 (Jackson laboratories, USA, (20)) were inoculated intranasally (I.N.) with 25 µL sterile  
275 Dulbecco's Modified Eagle Medium (DMEM) containing either 10<sup>4</sup> TCID<sub>50</sub> (low dose group, n =  
276 14), 10<sup>5</sup> TCID<sub>50</sub> (high dose group, n = 14) or 10<sup>5</sup> TCID<sub>50</sub> γ-irradiate (45) (control group, n = 2)  
277 SARS-CoV-2. At 3 and 7 DPI, four mice from the low dose and high dose groups were euthanized,  
278 respectively, and tissues were collected. The remaining mice were utilized for end-point data  
279 collection and survival assessment. Mice were weighed and nasal, oropharyngeal and rectal swabs  
280 were taken daily. Mice were observed for survival up to 21 DPI or until they reached end-point  
281 criteria. End-point criteria included several parameters of severe disease (increased respiratory  
282 rate, hunched posture, ruffled fur and lethargy).

283

284 **RNA extraction and quantitative reverse-transcription polymerase chain reaction**

285 Samples were collected with prewetted swabs in 1 mL of DMEM supplemented with 100 U/mL  
286 penicillin and 100 µg/mL streptomycin. Then, 140 µL was utilized for RNA extraction using the  
287 QIAamp Viral RNA Kit (Qiagen) using QIAcube HT automated system (Qiagen) according to the

288 manufacturer's instructions with an elution volume of 150  $\mu$ L. Tissues (up to 30 mg) were  
289 homogenized in RLT buffer and RNA was extracted using the RNeasy kit (Qiagen) according to  
290 the manufacturer's instructions. Viral RNA was detected by qRT-PCR (46). Five  $\mu$ L RNA was  
291 tested with the Rotor-Gene<sup>TM</sup> probe kit (Qiagen) according to instructions of the manufacturer.  
292 Ten-fold dilutions of SARS-CoV-2 standards with known copy numbers were used to construct a  
293 standard curve.

294

### 295 **SARS-CoV-2 spike glycoprotein enzyme-linked immunosorbent assay (ELISA)**

296 Maxisorp plates (Nunc) were coated with 50 ng spike protein per well and incubated overnight at  
297 4°C. After blocking with casein in phosphate buffered saline (PBS) (ThermoFisher) for 1 h at room  
298 temperature (RT), serially diluted 2-fold serum samples (duplicate, in casein) were incubated for  
299 1 h at RT. Spike-specific antibodies were detected with goat anti-mouse IgM or IgG Fc  
300 (horseradish peroxidase (HRP)-conjugated, Abcam) for 1 h at RT and visualized with KPL TMB  
301 2-component peroxidase substrate kit (SeraCare, 5120-0047). The reaction was stopped with KPL  
302 stop solution (Seracare) and read at 450 nm. Plates were washed 3x with PBS-T (0.1% Tween) in  
303 between steps. The threshold for positivity was calculated as the average plus 3x the standard  
304 deviation of negative control mouse sera.

305

### 306 **Measurement of cytokines and chemokines**

307 Serum samples were inactivated with  $\gamma$ -irradiation (2 mRad) and cytokine concentrations were  
308 determined on a Bio-Plex 200 instrument (Bio-Rad) using Milliplex Mouse Cytokine/Chemokine  
309 MAGNETIC BEAD Premixed 25 Plex Kit (Millipore), according to the manufacturer's  
310 instructions. Samples were pre-diluted 1:3 in the kit serum matrix (v:v). Concentrations below the

311 limit of detections were set to zero. Heatmap and correlation graphs were made in R (47) using  
312 pheatmap (48) and corrplot (49) packages.

313

### 314 **Histology and immunohistochemistry**

315 Necropsies and tissue sampling were performed according to IBC-approved protocols. Harvested  
316 tissues were fixed for eight days in 10% neutral-buffered formalin, embedded in paraffin,  
317 processed using a VIP-6 Tissue Tek (Sakura Finetek, USA) tissue processor, and embedded in  
318 Ultraffin paraffin polymer (Cancer Diagnostics, Durham, NC). Samples were sectioned at 5  $\mu$ m,  
319 and resulting slides were stained with hematoxylin and eosin. Specific anti-CoV immunoreactivity  
320 was detected using an in-house SARS-CoV-2 nucleocapsid protein rabbit antibody at a 1:1000  
321 dilution. Macrophage (CD68) and T-cell (CD3) immunoreactivities were detected using CD68  
322 rabbit polyclonal antibody (Abcam) at a 1:250 dilution and prediluted CD3 rabbit monoclonal  
323 antibody (2GV6, Roche Tissue Diagnostics), respectively. For both CD68 and CD3, ImmPRESS-  
324 VR Horse anti-rabbit polymer was used as the secondary antibody (Vector Laboratories). B-cell  
325 (CD45) immunoreactivity was detected using anti CD45R rat monoclonal antibody (Abcam) at a  
326 1:500 dilution and ImmPRESS goat anti-rat polymer (Vector Laboratories) as secondary  
327 antibody. The immunohistochemistry (IHC) assay was carried out on a Discovery ULTRA  
328 automated staining instrument (Roche Tissue Diagnostics) with a Discovery ChromoMap DAB  
329 (Ventana Medical Systems) kit. All tissue slides were evaluated by a board-certified veterinary  
330 anatomic pathologist blinded to study group allocations.

331

### 332 **Statistical analyses**

333 Two-tailed Mann-Whitney's rank tests and Wilcoxon matched-pairs rank test were conducted to  
334 compare differences between groups.

335

## 336 **Acknowledgements**

337 The authors would like to thank Nathalie Thornburg and Susan Gerber for sharing of the SARS-  
338 CoV-2 isolate, Kizzmekia Corbett and Barney Graham for the plasmid encoding the full-length  
339 SARS-CoV-2 spike and Anita Mora for assistance with the Figs. This work was supported by the  
340 Intramural Research Program of the National Institute of Allergy and Infectious Diseases (NIAID),  
341 National Institutes of Health (NIH) (1ZIAAI001179-01).

342

## 343 **References**

- 344 1. WHO. Coronavirus disease 2019 (COVID-19) Situation Report – 52. 2020 12 March 2020.
- 345 2. Nie S, Han S, Ouyang H, Zhang Z. Coronavirus Disease 2019-related dyspnea cases difficult to interpret  
346 using chest computed tomography. *Respir Med.* 2020;167:105951-.
- 347 3. Parry AH, Wani AH, Yaseen M, Dar KA, Choh NA, Khan NA, et al. Spectrum of chest computed  
348 tomographic (CT) findings in coronavirus disease-19 (COVID-19) patients in India. *Eur J Radiol.* 2020;129:109147-  
349 .
- 350 4. Li X, Ma X. Acute respiratory failure in COVID-19: is it "typical" ARDS? *Crit Care.* 2020;24(1):198.
- 351 5. Jiang F, Deng L, Zhang L, Cai Y, Cheung CW, Xia Z. Review of the Clinical Characteristics of  
352 Coronavirus Disease 2019 (COVID-19). *J Gen Intern Med.* 2020;35(5):1545-9.
- 353 6. Li X, Ma X. Acute respiratory failure in COVID-19: is it "typical" ARDS? *Crit Care.* 2020;24(1):198-.
- 354 7. Calcagno N, Colombo E, Maranzano A, Pasquini J, Keller Sarmiento IJ, Trogu F, et al. Rising evidence for  
355 neurological involvement in COVID-19 pandemic. *Neurol Sci.* 2020;41(6):1339-41.
- 356 8. Dhakal BP, Sweitzer NK, Indik JH, Acharya D, William P. SARS-CoV-2 Infection and Cardiovascular  
357 Disease: COVID-19 Heart. *Heart Lung Circ.* 2020.
- 358 9. Mao L, Jin H, Wang M, Hu Y, Chen S, He Q, et al. Neurologic Manifestations of Hospitalized Patients  
359 With Coronavirus Disease 2019 in Wuhan, China. *JAMA Neurol.* 2020.
- 360 10. Chan JF, Zhang AJ, Yuan S, Poon VK, Chan CC, Lee AC, et al. Simulation of the clinical and pathological  
361 manifestations of Coronavirus Disease 2019 (COVID-19) in golden Syrian hamster model: implications for disease  
362 pathogenesis and transmissibility. *Clin Infect Dis.* 2020.

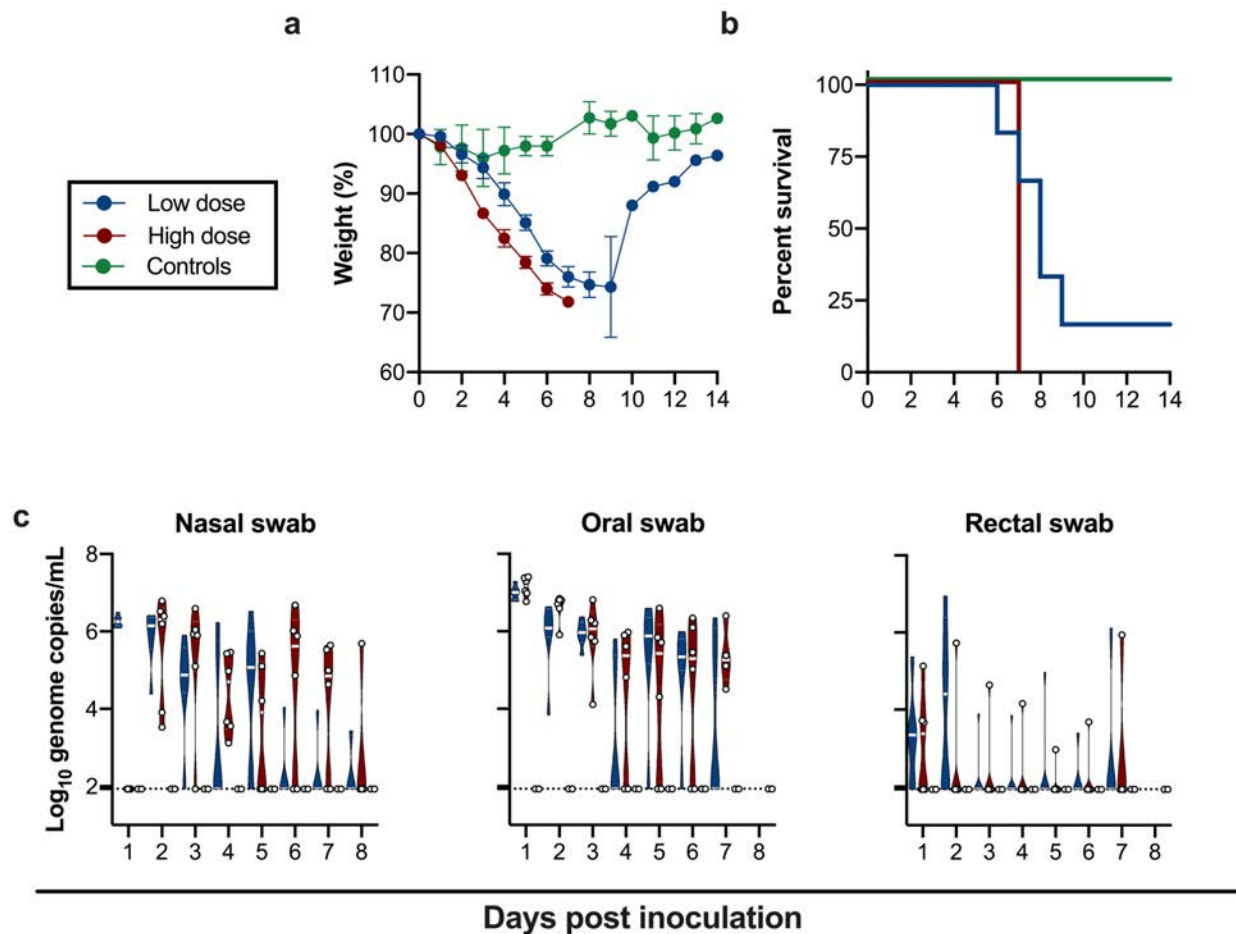


- 363 11. Kim YI, Kim SG, Kim SM, Kim EH, Park SJ, Yu KM, et al. Infection and Rapid Transmission of SARS-  
364 CoV-2 in Ferrets. *Cell Host Microbe*. 2020;27(5):704-9 e2.
- 365 12. Munster VJ, Feldmann F, Williamson BN, van Doremalen N, Perez-Perez L, Schulz J, et al. Respiratory  
366 disease in rhesus macaques inoculated with SARS-CoV-2. *Nature*. 2020.
- 367 13. Woolsey C, Borisevich V, Prasad AN, Agans KN, Deer DJ, Dobias NS, et al. Establishment of an African  
368 green monkey model for COVID-19. *bioRxiv*. 2020.
- 369 14. Yu P, Qi F, Xu Y, Li F, Liu P, Liu J, et al. Age-related rhesus macaque models of COVID-19. *Animal  
370 Model Exp Med*. 2020;3(1):93-7.
- 371 15. Rockx B, Kuiken T, Herfst S, Bestebroer T, Lamers MM, Oude Munnink BB, et al. Comparative  
372 pathogenesis of COVID-19, MERS, and SARS in a nonhuman primate model. *Science*. 2020;368(6494):1012-5.
- 373 16. Letko M, Marzi A, Munster V. Functional assessment of cell entry and receptor usage for SARS-CoV-2  
374 and other lineage B betacoronaviruses. *Nature microbiology*. 2020;5(4):562-9.
- 375 17. Zhou P, Yang XL, Wang XG, Hu B, Zhang L, Zhang W, et al. A pneumonia outbreak associated with a  
376 new coronavirus of probable bat origin. *Nature*. 2020;579(7798):270-3.
- 377 18. Zhao X, Chen D, Szabla R, Zheng M, Li G, Du P, et al. Broad and differential animal ACE2 receptor usage  
378 by SARS-CoV-2. *bioRxiv*. 2020.
- 379 19. Jing Sun, Zhuang Z, Zheng J, Li K, Wong RL-Y, Liu D, et al. Generation of a Broadly Useful Model for  
380 COVID-19 Pathogenesis, Vaccination, and Treatment. *Cell*. 2020.
- 381 20. McCray PB, Jr., Pewe L, Wohlford-Lenane C, Hickey M, Manzel L, Shi L, et al. Lethal infection of K18-  
382 hACE2 mice infected with severe acute respiratory syndrome coronavirus. *J Virol*. 2007;81(2):813-21.
- 383 21. Sun SH, Chen Q, Gu HJ, Yang G, Wang YX, Huang XY, et al. A Mouse Model of SARS-CoV-2 Infection  
384 and Pathogenesis. *Cell Host Microbe*. 2020.
- 385 22. Hongjing Gu, Chen Q, Yang G, He L, Fan H, Deng Y-Q, et al. Rapid adaption of SARS-CoV-2 in BALB/c  
386 mice: Novel mouse model for vaccine efficacy. *BioRxiv*. May 2, 2020.
- 387 23. Dinno KH, Leist SR, Schafer A, Edwards CE, Martinez DR, Montgomery SA, et al. A mouse-adapted  
388 SARS-CoV-2 model for the evaluation of COVID-19 medical countermeasures. *bioRxiv*. 2020.
- 389 24. Rojas JM, Avia M, Martín V, Sevilla N. IL-10: A Multifunctional Cytokine in Viral Infections. *J Immunol  
390 Res*. 2017;2017:6104054-.
- 391 25. Chen G, Wu D, Guo W, Cao Y, Huang D, Wang H, et al. Clinical and immunological features of severe  
392 and moderate coronavirus disease 2019. *J Clin Invest*. 2020;130(5):2620-9.
- 393 26. Bao L, Deng W, Huang B, Gao H, Liu J, Ren L, et al. The pathogenicity of SARS-CoV-2 in hACE2  
394 transgenic mice. *Nature*. 2020.
- 395 27. Hassan AO, Case JB, Winkler ES, Thackray LB, Kafai NM, Bailey AL, et al. A SARS-CoV-2 Infection  
396 Model in Mice Demonstrates Protection by Neutralizing Antibodies. *Cell*. 2020.
- 397 28. Jiang RD, Liu MQ, Chen Y, Shan C, Zhou YW, Shen XR, et al. Pathogenesis of SARS-CoV-2 in  
398 Transgenic Mice Expressing Human Angiotensin-Converting Enzyme 2. *Cell*. 2020.

- 399 29. Israelow B, Song E, Mao T, Lu P, Meir A, Liu F, et al. Mouse model of SARS-CoV-2 reveals  
400 inflammatory role of type I interferon signaling. *bioRxiv*. 2020:2020.05.27.118893.
- 401 30. Golden JW, Cline CR, Zeng X, Garrison AR, Carey BD, Mucker EM, et al. Human angiotensin-converting  
402 enzyme 2 transgenic mice infected with SARS-CoV-2 develop severe and fatal respiratory disease. *bioRxiv*.  
403 2020:2020.07.09.195230.
- 404 31. Moreau GB, Burgess SL, Sturek JM, Donlan AN, Petri WA, Mann BJ. Evaluation of K18-  
405 *hACE2* mice as a model of SARS-CoV-2 infection. *bioRxiv*. 2020:2020.06.26.171033.
- 406 32. Tian S, Hu W, Niu L, Liu H, Xu H, Xiao S-Y. Pulmonary Pathology of Early-Phase 2019 Novel  
407 Coronavirus (COVID-19) Pneumonia in Two Patients With Lung Cancer. *J Thorac Oncol*. 2020;15(5):700-4.
- 408 33. Schaller T, Hirschi K, Burkhardt K, Braun G, Trepel M, Märkl B, et al. Postmortem Examination of  
409 Patients With COVID-19. *JAMA*. 2020;323(24):2518-20.
- 410 34. Fox SE, Akmatbekov A, Harbert JL, Li G, Brown JQ, Vander Heide RS. Pulmonary and Cardiac Pathology  
411 in Covid-19: The First Autopsy Series from New Orleans. *medRxiv*. 2020:2020.04.06.20050575.
- 412 35. Yang Y, Shen C, Li J, Yuan J, Wei J, Huang F, et al. Plasma IP-10 and MCP-3 levels are highly associated  
413 with disease severity and predict the progression of COVID-19. *J Allergy Clin Immunol*. 2020;146(1):119-27.e4.
- 414 36. Liu Y, Zhang C, Huang F, Yang Y, Wang F, Yuan J, et al. Elevated plasma levels of selective cytokines in  
415 COVID-19 patients reflect viral load and lung injury. *National Science Review*. 2020;7(6):1003-11.
- 416 37. Wan S, Yi Q, Fan S, Lv J, Zhang X, Guo L, et al. Characteristics of lymphocyte subsets and cytokines in  
417 peripheral blood of 123 hospitalized patients with 2019 novel coronavirus pneumonia (NCP). *medRxiv*.  
418 2020:2020.02.10.20021832.
- 419 38. Sun S-H, Chen Q, Gu H-J, Yang G, Wang Y-X, Huang X-Y, et al. A Mouse Model of SARS-CoV-2  
420 Infection and Pathogenesis. *Cell host & microbe*. 2020;28(1):124-33.e4.
- 421 39. Ye Q, Wang B, Mao J. The pathogenesis and treatment of the 'Cytokine Storm' in COVID-19. *J Infect*.  
422 2020;80(6):607-13.
- 423 40. Huang C, Wang Y, Li X, Ren L, Zhao J, Hu Y, et al. Clinical features of patients infected with 2019 novel  
424 coronavirus in Wuhan, China. *The Lancet*. 2020;395(10223):497-506.
- 425 41. Chen L, Liu HG, Liu W, Liu J, Liu K, Shang J, et al. [Analysis of clinical features of 29 patients with 2019  
426 novel coronavirus pneumonia]. *Zhonghua Jie He He Hu Xi Za Zhi*. 2020;43(0):E005.
- 427 42. Wang H, Ma S. The cytokine storm and factors determining the sequence and severity of organ dysfunction  
428 in multiple organ dysfunction syndrome. *Am J Emerg Med*. 2008;26(6):711-5.
- 429 43. Parsons PE, Eisner MD, Thompson BT, Matthay MA, Ancukiewicz M, Bernard GR, et al. Lower tidal  
430 volume ventilation and plasma cytokine markers of inflammation in patients with acute lung injury. *Crit Care Med*.  
431 2005;33(1):1-6; discussion 230-2.
- 432 44. Girija ASS, Shankar EM, Larsson M. Could SARS-CoV-2-Induced Hyperinflammation Magnify the  
433 Severity of Coronavirus Disease (CoViD-19) Leading to Acute Respiratory Distress Syndrome? *Frontiers in*  
434 *Immunology*. 2020;11(1206).
- 435 45. Feldmann F, Shupert WL, Haddock E, Twardoski B, Feldmann H. Gamma Irradiation as an Effective  
436 Method for Inactivation of Emerging Viral Pathogens. *The American journal of tropical medicine and hygiene*.  
437 2019;100(5):1275-7.

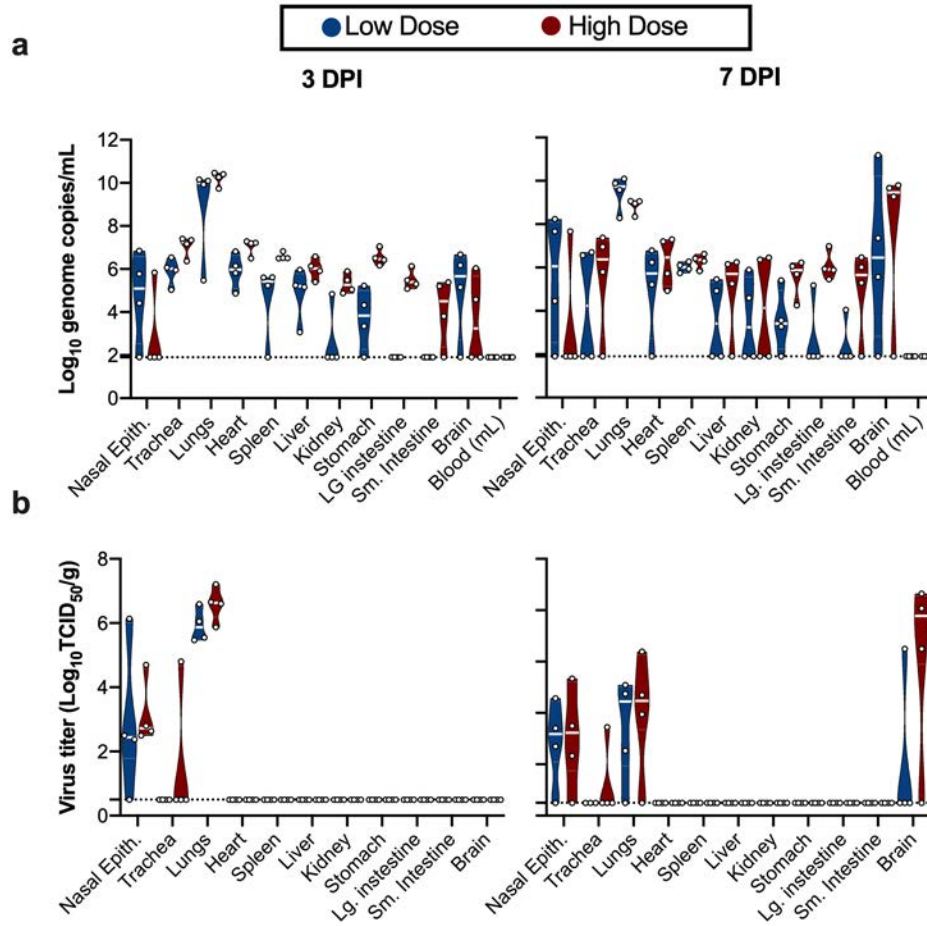
- 438 46. Corman VM, Landt O, Kaiser M, Molenkamp R, Meijer A, Chu DK, et al. Detection of 2019 novel  
439 coronavirus (2019-nCoV) by real-time RT-PCR. *Euro Surveill.* 2020;25(3).
- 440 47. R Development Core Team. R: A language and Environment for Statistical computing R Foundation for  
441 Statistical Computing; 2010.
- 442 48. Kolde R. Implementation of heatmaps that offers more control over dimensions and appearance. 2019.
- 443 49. Wei T, Simko V. R package "corrplot": Visualization of a Correlation Matrix. Version 0.84 ed2017.
- 444

## 445 Figures



446

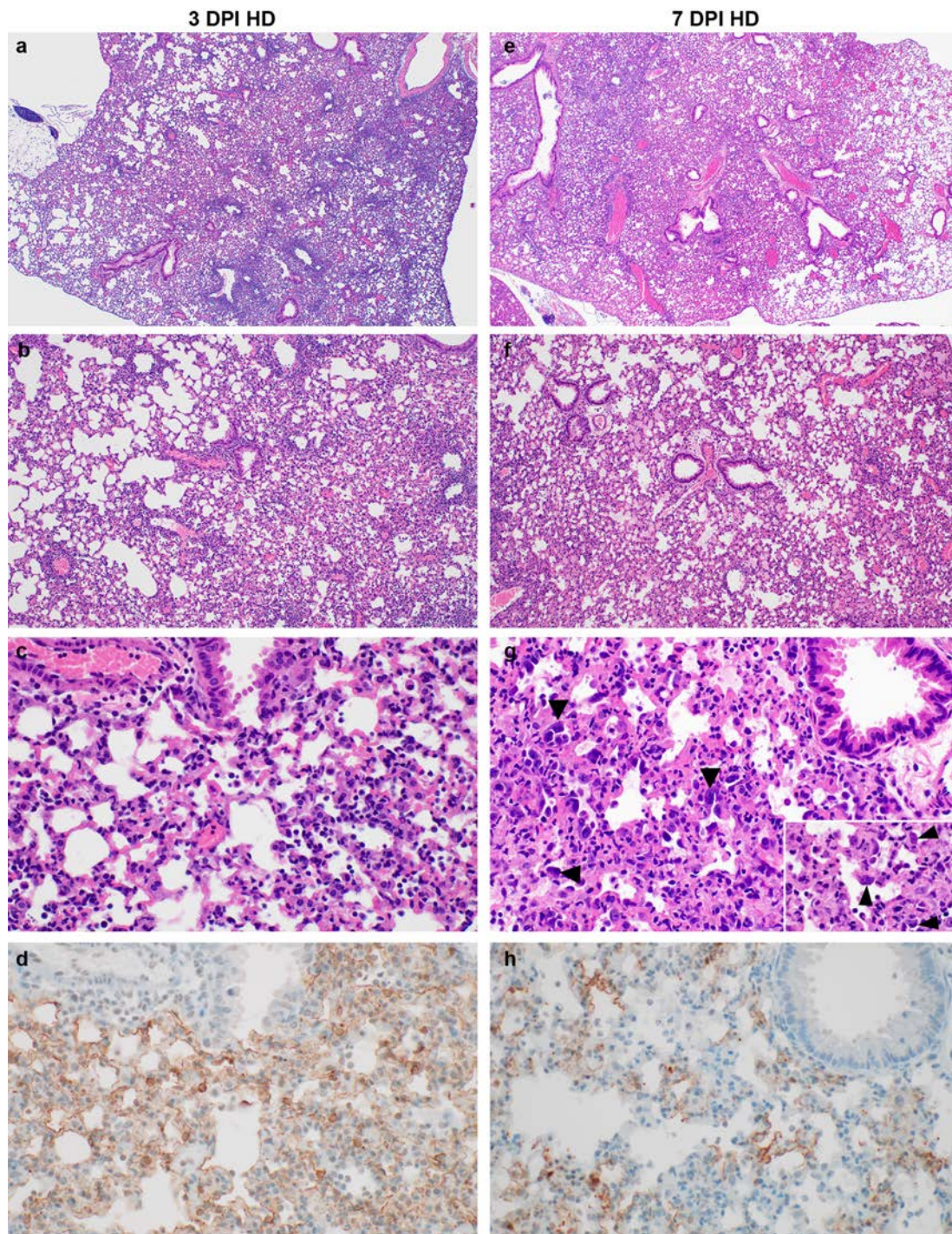
447 **Fig 1. Inoculation of K18-hACE2 mice results in lethal infection and virus shedding**



448

449 **Fig 2. SARS-CoV-2 tissue tropism in K18-hACE mice.**

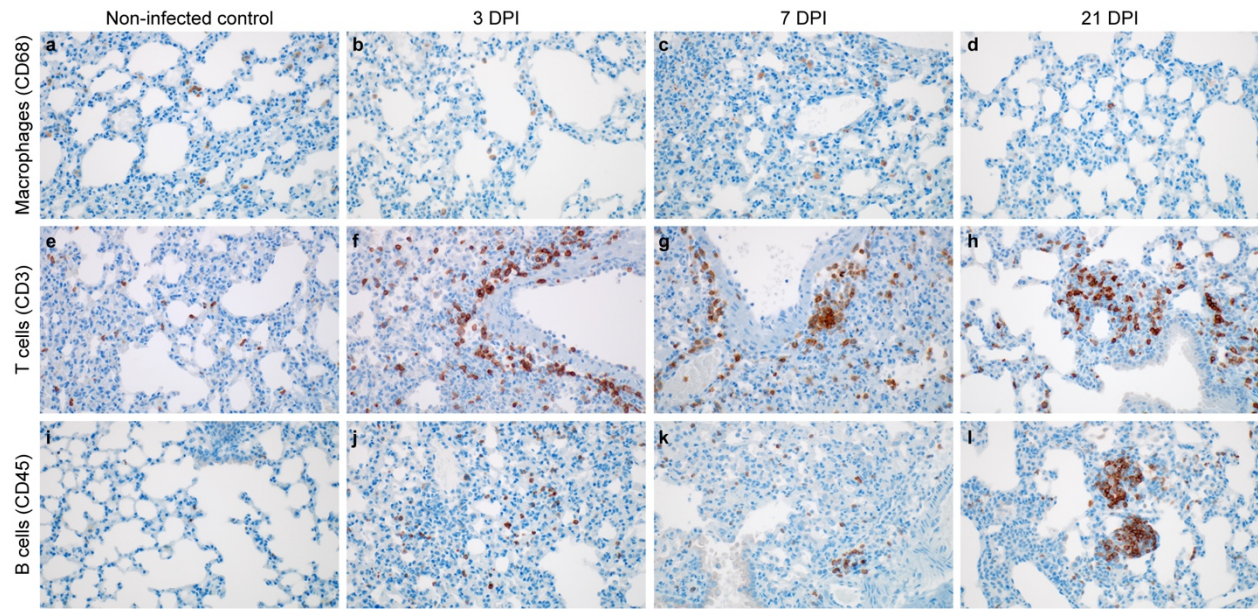




450

451 **Fig 3. Pathological changes in lungs of K18-hACE mice inoculated with SARS-CoV-2 at 3**  
452 **and 7 DPI.**



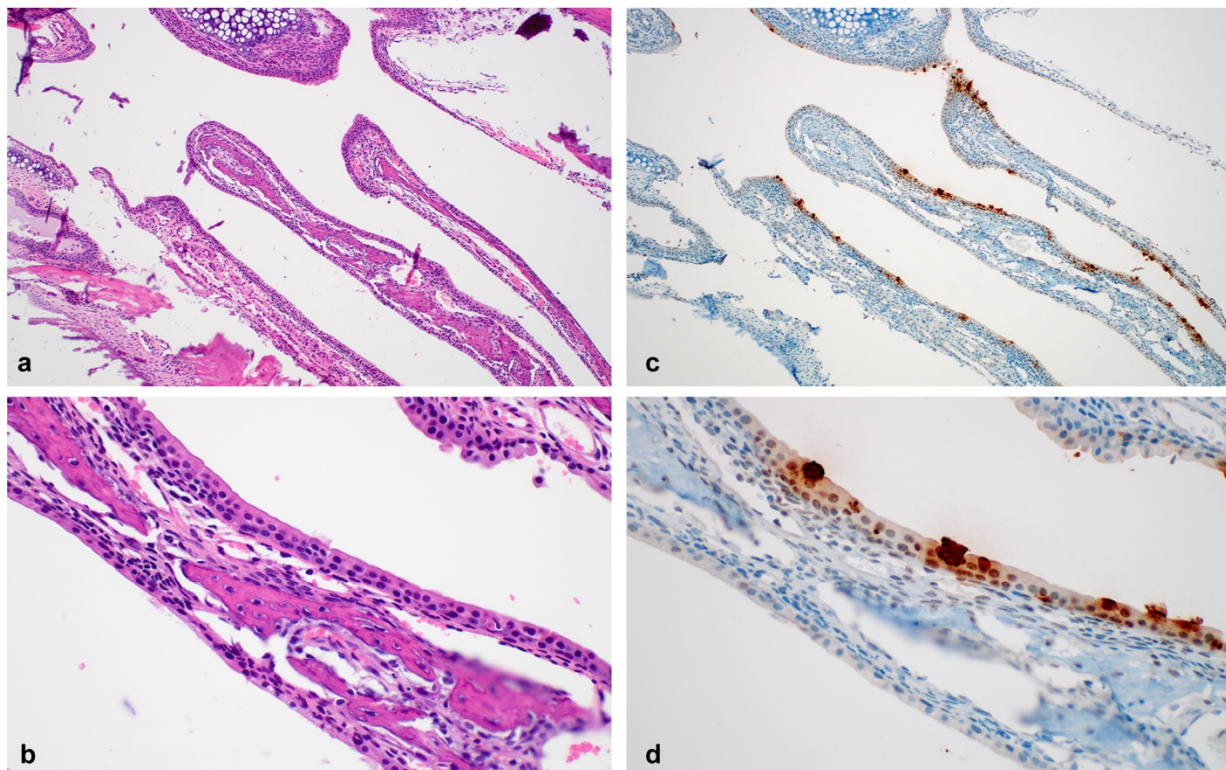


453

454 **Fig 4. Infiltration of innate and adaptive immune-cell populations in the lungs of SARS-**

455 **CoV-2 infected mice.**

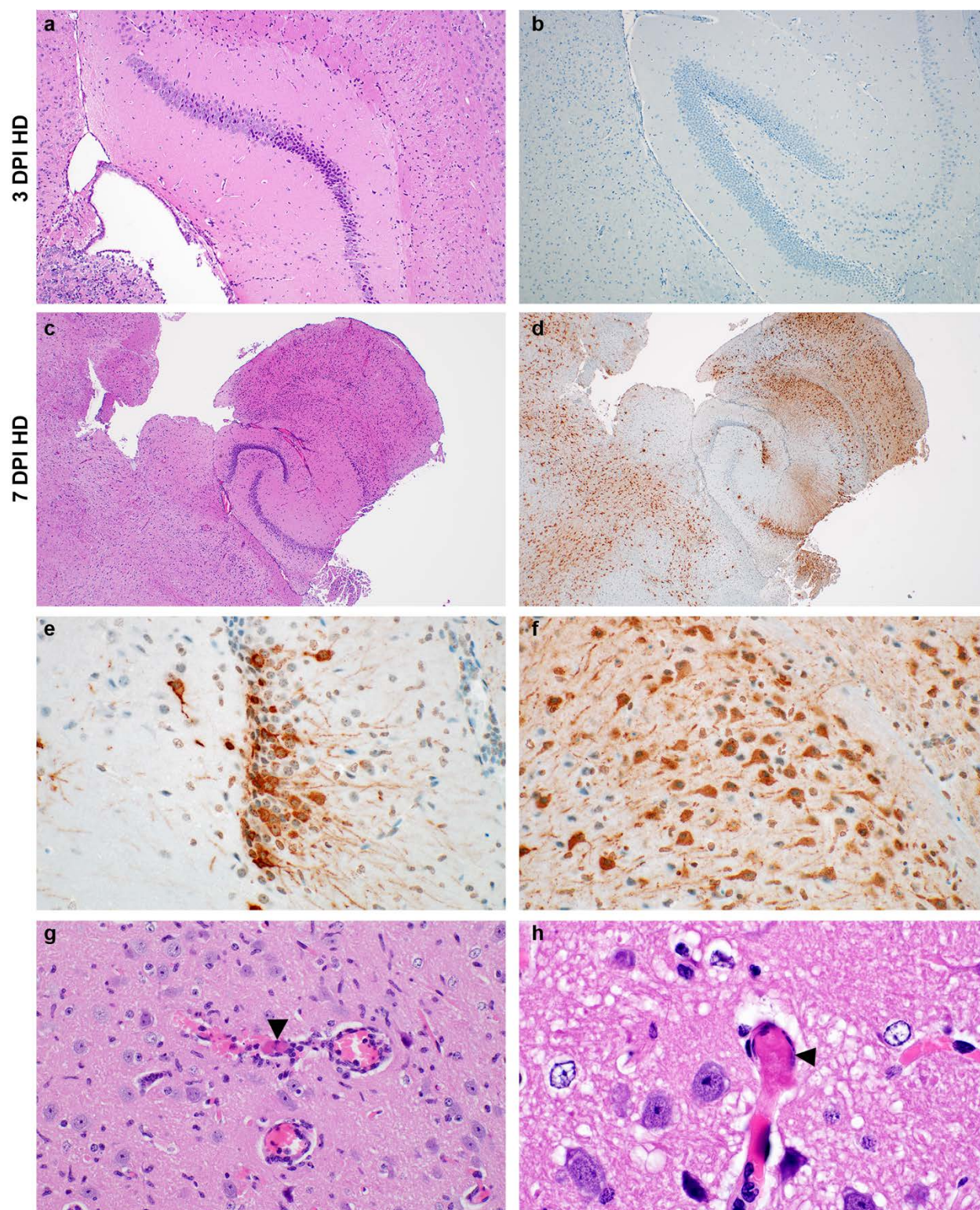
456



457

458 **Fig 5. Pathological changes in nasal turbinates in SARS-CoV-2 infected mice.**

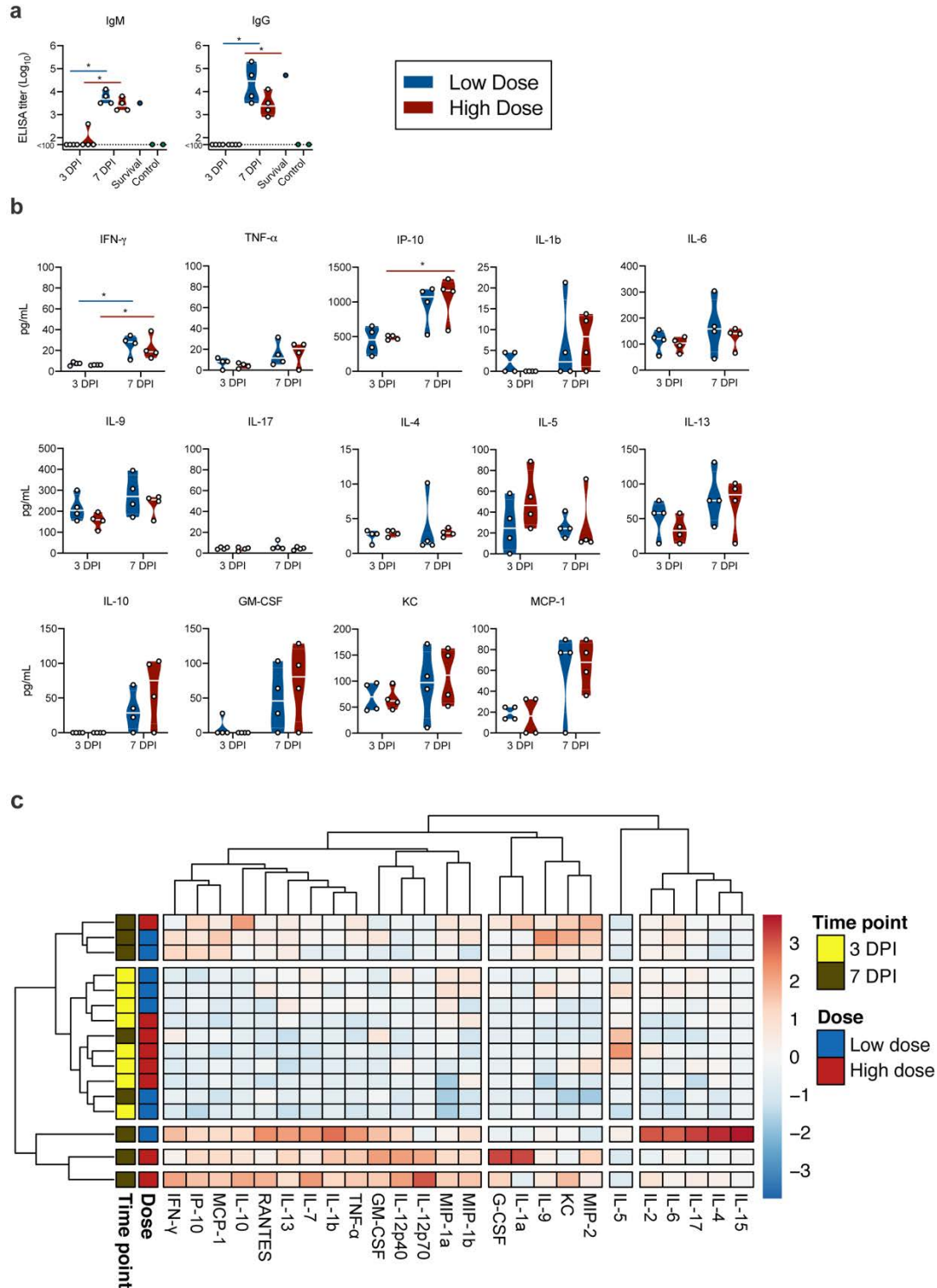




459

460 **Fig 6. Neurotropism of SARS-CoV-2 in infected mice at 7 DPI. a and b.**

461



462

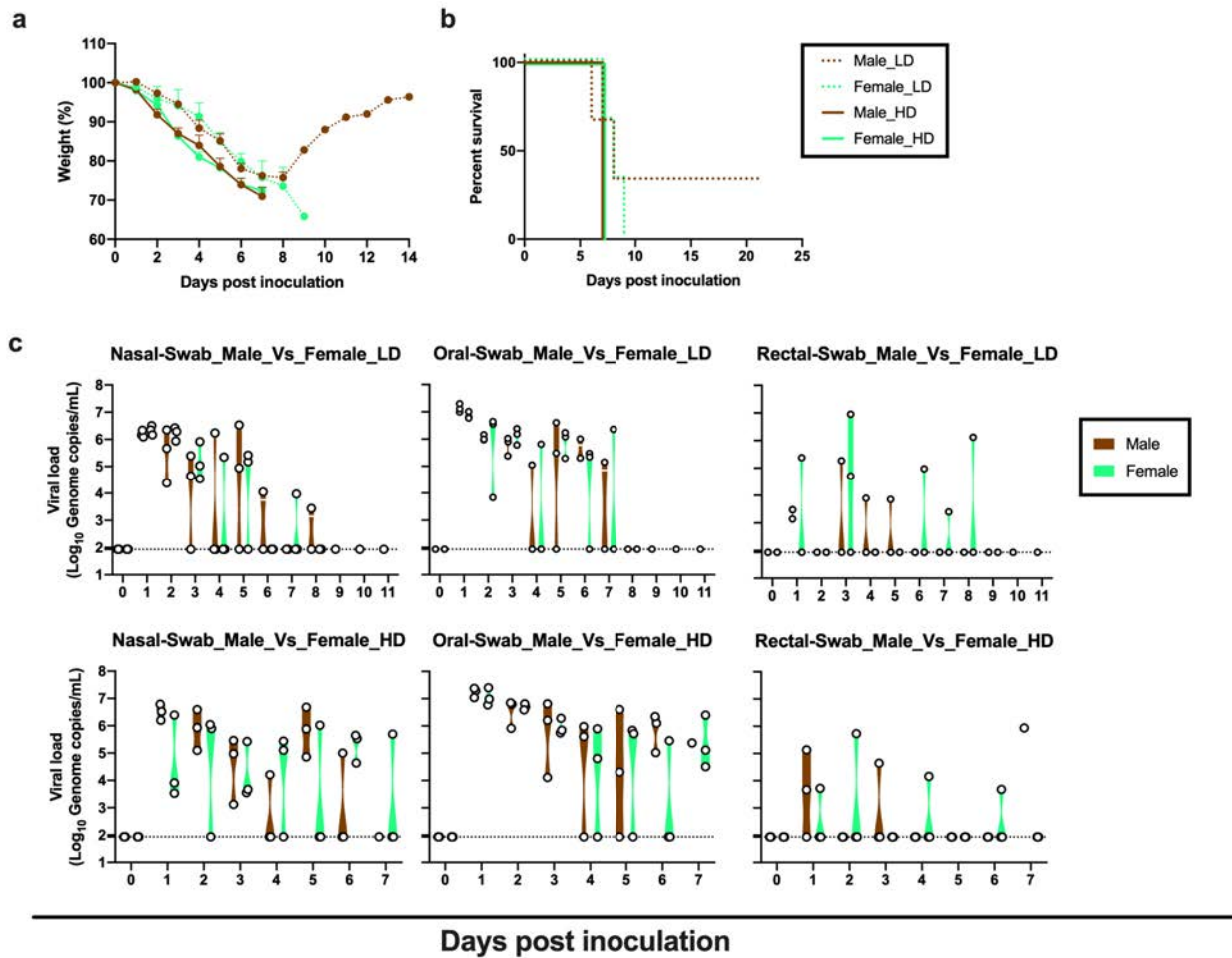
463 **Fig 7. Humoral and cytokine/chemokine responses to SARS-CoV-2 infection in K18-hACE**

464 **mice.**

465



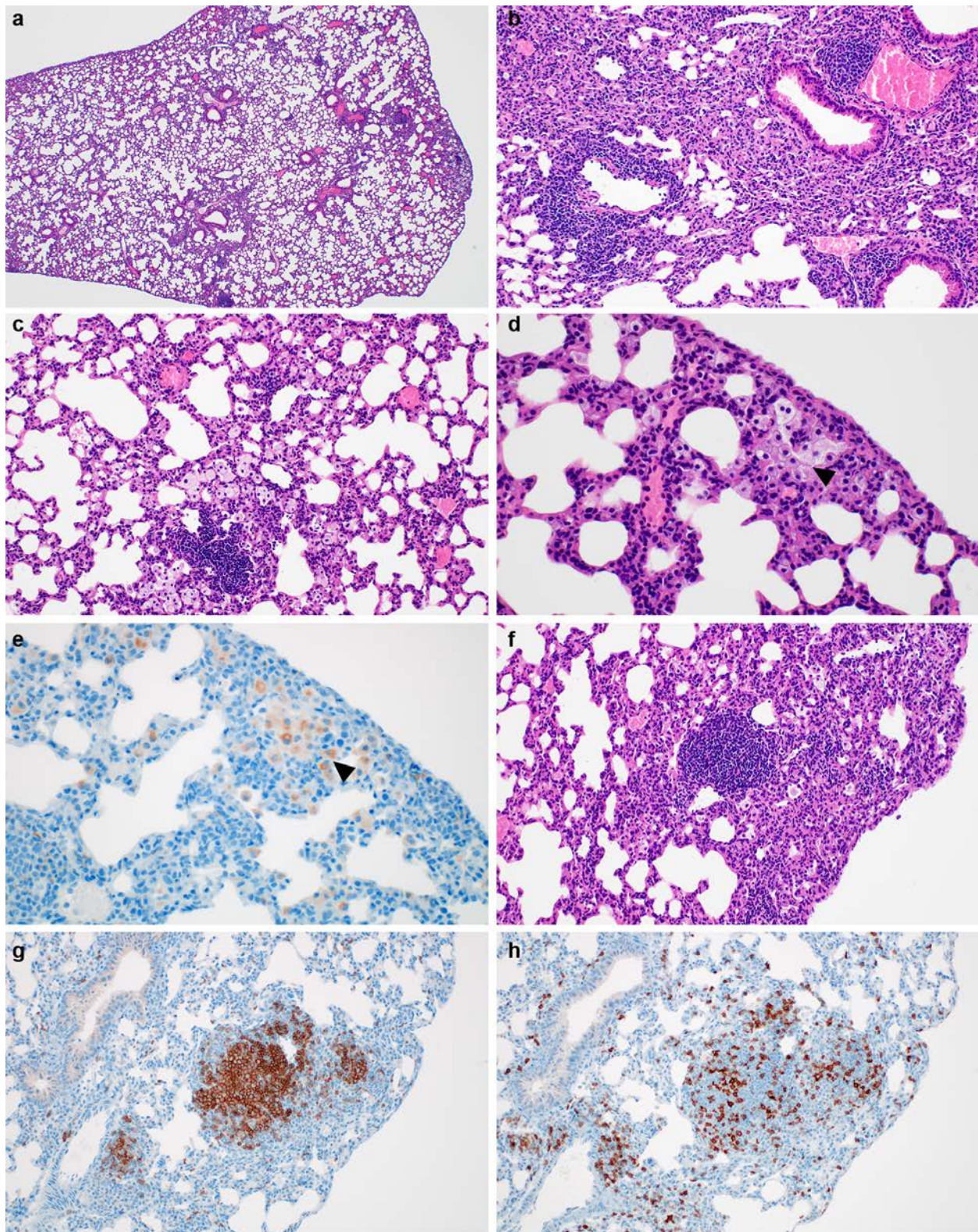
466 **Supplementary Figures**  
467  
468



469  
470 **S1 Fig. Sex-dependent weight loss, mortality and virus shedding in K18-hACE2 mice after**  
471 **SARS-CoV-2 infection**

472

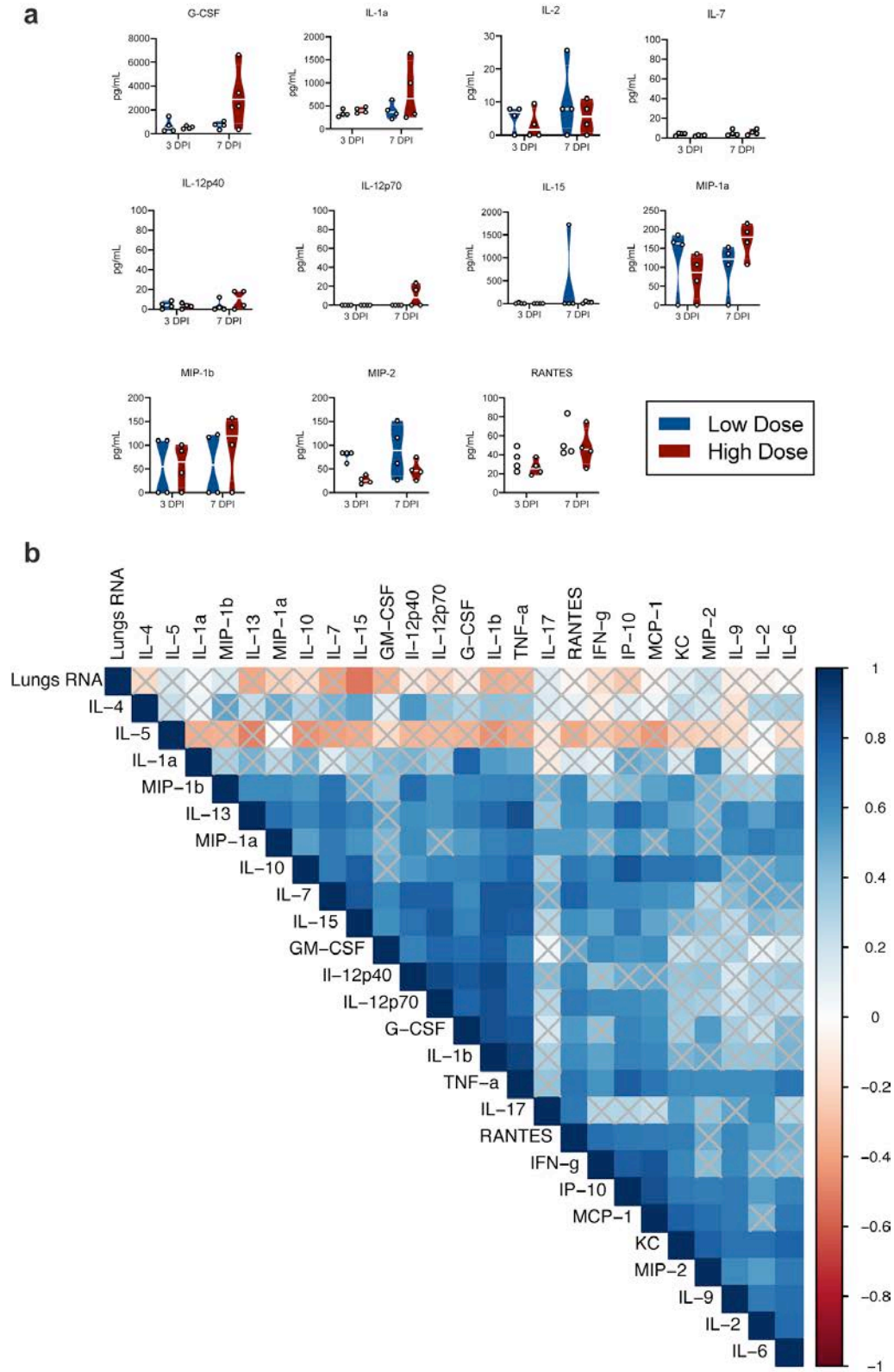




473  
474  
475  
476  
477

**S2 Fig. Histological analysis of lung sections from one low dose survivor at 21 days post infection**





478  
479  
480  
481

**S3 Fig. Multiplex analysis of cytokines/chemokines in K18-hACE mice challenged with SARS-CoV-2**

## 482 **Figure Legends**

483 **Fig 1. Inoculation of K18-hACE2 mice results in lethal infection and virus shedding. a.**  
484 Relative weight loss in mice after SARS-CoV-2 inoculation. The lines represent mean  $\pm$  SEM. **b.**  
485 Survival curves of mice inoculated with  $10^4$  or  $10^5$  TCID<sub>50</sub> SARS-CoV-2, or  $10^5$   $\gamma$ -irradiated  
486 SARS-CoV-2. **c.** Violin plot of viral load in nasal, oropharyngeal and rectal swabs with geometric  
487 mean as centre. Viral RNA was quantified using RT-qPCR in nasal, oropharyngeal and rectal  
488 swabs, bar at geometric mean. Blue:  $10^4$  TCID<sub>50</sub> (low dose animals, n = 6); red:  $10^5$  TCID<sub>50</sub> (high  
489 dose animals, n = 6); green:  $10^5$  TCID<sub>50</sub>  $\gamma$ -irradiated (control animals, n = 2); dotted line = limit of  
490 detection.

491  
492 **Fig 2. SARS-CoV-2 tissue tropism in K18-hACE mice. a.** Violin plot of viral load in tissues  
493 quantified by UpE RT-qPCR with geometric mean as center. **b.** Violin plot of infectious SARS-  
494 CoV-2 titers in tissues, with geometric mean as centre. Blue:  $10^4$  TCID<sub>50</sub> (low dose animals, n =  
495 6); red:  $10^5$  TCID<sub>50</sub> (high dose animals, n = 6); green:  $10^5$  TCID<sub>50</sub>  $\gamma$ -irradiated (control animals, n  
496 = 2); dotted line = limit of detection.

497  
498 **Fig 3. Pathological changes in lungs of K18-hACE mice inoculated with SARS-CoV-2 at 3**  
499 **and 7 DPI. a, b, c.** Interstitial pneumonia at 3 DPI, characterized by perivascular and septal  
500 inflammation with neutrophils, macrophages, lymphocytes, and edema. **d.** SARS-CoV-2 antigen  
501 immunoreactivity at 3 DPI in alveolar pneumocytes and macrophages. **e, f, g.** Multifocal interstitial  
502 pneumonia at 7 DPI, characterized by type II pneumocyte hyperplasia (arrowheads), alveolar and  
503 perivascular inflammation, fibrin, edema, syncytial cells (insert arrowheads), and single cell  
504 necrosis. **h.** SARS-CoV-2 antigen immunoreactivity in pneumocytes and macrophages at 7 DPI.  
505 HD: high dose ( $10^5$  TCID<sub>50</sub> SARS-CoV-2). Magnification: a, e = 40 x; b, f = 100 x; c, g,h = 400  
506 x, inset 1000 x.

507  
508 **Fig 4. Infiltration of innate and adaptive immune-cell populations in the lungs of SARS-CoV-**  
509 **2 infected mice. a-c. a, e, i.**  $\gamma$ -irradiated SARS-CoV-2 inoculated controls. **b, f, j.**  $10^5$  TCID<sub>50</sub> 3  
510 DPI. **c, g, k,**  $10^5$  TCID<sub>50</sub> 7 PDI. **d, h, l.** survivor animal 21 DPI. **a.** Controls (animals inoculated  
511 with  $\gamma$ -irradiated SARS-CoV-2) with few macrophages (brown). **b, c.** Increased macrophages  
512 (brown) at 3 and 7 DPI. **d.** Macrophages (brown) present at end of study in a surviving mouse. **e.**

513 Scattered T cells (brown) in the non infected control. **f, g.** T cells (brown) are increased in  
514 perivascular tissue and alveolar septa at 3 and 7 DPI. **h.** T cells (brown) forming lymphoid  
515 aggregates with B cells in perivascular tissues. **i.** B cells (brown) are few in the non infected  
516 control. **j and k.** B cells (brown) are increased in alveolar septa at 3 and 7 DPI. **l.** B cells (brown)  
517 forming lymphoid aggregates with T cells in perivascular tissues. Magnification: a-l = 400 x.

518

519 **Fig 5. Pathological changes in nasal turbinates of SARS-CoV-2 infected mice.** **a.** Nasal  
520 turbinates lined by respiratory epithelium **b.** SARS-CoV-2 antigen (brown) visible in respiratory  
521 epithelial cells. **c.** nasal turbinates without inflammation. **d.** Viral antigen in the cytoplasm of  
522 ciliated respiratory epithelial cells. Magnification: a, c = 100 x; b, d = 400 x.

523

524 **Fig 6. Neurotropism of SARS-CoV-2 in infected mice at 7 DPI.** **a and b.** Normal hippocampus  
525 with no SARS-CoV-2 antigen detected at 3 DPI. **c.** Generalized increase in cellularity of the  
526 cerebral cortex and hippocampus; meninges are mildly expanded by edema and inflammatory cells  
527 at 7 DPI. **d.** SARS-CoV-2 antigen (brown) visible throughout the cerebral cortex and hippocampus  
528 at 7 DPI. **e and f.** SARS-CoV-2 antigen in neurons of the hippocampus and cerebral cortex  
529 highlights the soma and axons at 7 DPI. **g.** A small caliber vessel in the cerebral cortex contains a  
530 microthrombus (arrowheads) surrounded by hemorrhage and inflammatory cells which infiltrate  
531 the adjacent neuropil; there are increased glial cells throughout the image. **h.** Another  
532 microthrombus (arrowheads) in a small caliber vessel. a-b = 3 DPI, c-h = 7 DPI, dose group =  $10^5$   
533 TCID<sub>50</sub> SARS-CoV-2. Magnification: a, b = 100 x; c, d = 40 x; e-g 400 x; and h = 1000 x.

534

535 **Fig 7. Humoral and cytokine/chemokine responses to SARS-CoV-2 infection in K18-hACE**  
536 **mice.** **a.** IgM and IgG antibody titres against SARS-CoV-2 spike ectodomain by ELISA in serum.  
537 White line represents geometric mean of end point dilutions per study group. Dotted line represents  
538 limit of detection. **b.** Four-fold serial-diluted serum of selected cytokines/chemokines in K18-  
539 hACE mice challenged with SARS-CoV-2 measured on Bio-Plex 200 instrument (Bio-Rad)  
540 using Milliplex Mouse Cytokine/Chemokine MAGNETIC BEAD Premixed 25 Plex  
541 Kit (Millipore). Whitened represent geometric mean of all mice. **c.** Heatmap showing cytokine  
542 titers clusters based on DPI and dose of inoculation.

543

544 **Supplementary Figure legends**

545 **S1 Fig. Sex-dependent weight loss, mortality and virus shedding in K18-hACE2 mice after**  
546 **SARS-CoV-2 infection. a.** Body weights were monitored every day. Relative body weight  
547 changes are show for female (turquoise) and male (brown) animals for HD (solid) and LD (dotted)  
548 groups. **b.** Survival is show for female (turquoise) and male (brown) animals for HD (solid) and  
549 LD (dotted) groups. **c.** Nasal, oral and rectal virus shedding in low and high dose infected female  
550 (turquoise) and male (brown) mice was quantified by RT-qPCR across time. Individual animals  
551 are plotted, violin plot depict median and quantiles. Abbreviations: LD = low dose ( $10^4$  TCID<sub>50</sub>  
552 SARS-CoV-2), HD = high dose ( $10^5$  TCID<sub>50</sub> SARS-CoV-2).

553  
554 **S2 Fig. Histological analysis of lung sections from one low dose survivor at 21 days post**  
555 **infection. a.** Multiple foci of perivascular inflammation and increased alveolar cellularity. **b.**  
556 Perivascular and peribronchiolar lymphocytic inflammation. **c.** Aggregated lymphocytes within  
557 alveolar septa and alveoli containing foamy macrophages. **d.** Foamy macrophages cluster and fill  
558 alveoli (arrowheads) and alveolar septa contain increased numbers of lymphocytes. **e.** CD68  
559 immunoreactivity in foamy alveolar macrophages (arrowheads). **f.** One of many discreet  
560 aggregates of lymphocytes in the 21 DPI lung composed of **g.** CD45<sup>+</sup> B cells and **h.** CD3<sup>+</sup> T cells.  
561 Magnification: a = 40 x; b, c, f, g, h = 200 x; d, e = 400 x.

562  
563 **S3 Fig. Multiplex analysis of cytokines/chemokines in K18-hACE mice challenged with**  
564 **SARS-CoV-2 measured at 3- and 7-days post inoculation. a.** Individual animals are plotted,  
565 violin plots depict median and quantiles. Low dose = blue, high dose = red. **b.** Correlation between  
566 cytokine levels and viral RNA in the lungs. Significant correlations ( $p = 0.05$ ) are shown and  
567 strength of correlation is depicted according to the colour bar, crossed bars are not significant.  
568 Abbreviations: DPI = days post inoculation, G-CSF = granulocyte colony-stimulating factor, GM-  
569 CSF = granulocyte-macrophage colony-stimulating factor, INF = interferon, IL = interleukin, KC  
570 = keratinocyte chemoattractant, MCP = monocyte chemoattractant protein, MIP = macrophage  
571 inflammatory protein, IP = interferon- $\gamma$ -inducible protein, TNF = tumour necrosis factor.